ISSN 1674-1056
http://cpb.iphy.ac.cn
http://iopscience.iop.org/cpb
中国物理 B
Chinese Physics
中国物理
Chinese Physics B

Visible-to-near-infrared photodetector based on graphene-$MoTe_2$-graphere heterostructure

Rui-Xue Hu(户瑞雪), Xin-Li Ma(马新莉), Chun-Ha An(安春华), Jing Liu(刘晶)
Citation: Chin. Phys. B . 2019, 28(11): 117802 . **doi:** 10.1088/1674-1056/ab4576
Journal homepage: http://cpb.iphy.ac.cn; http://iopscience.iop.org/cpb

What follows is a list of articles you may be interested in

Efficient doping modulation of monolayer WS_2 for optoelectronic applications

Xinli Ma(马新莉), Rongjie Zhang(张荣杰), Chunhua An(安春华), Sen Wu(吴森), Xiaodong Hu(胡晓东), Jing Liu(刘晶)
Chin. Phys. B . 2019, 28(3): 037803 . **doi:** 10.1088/1674-1056/28/3/037803

Raman spectroscopy characterization of two-dimensional materials

Fang Liang(梁芳), Hejun Xu(徐何军), Xing Wu(吴幸), Chaolun Wang(王超伦), Chen Luo(骆晨), Jian Zhang(张健)
Chin. Phys. B . 2018, 27(3): 037802 . **doi:** 10.1088/1674-1056/27/3/037802

Optical response of tunable terahertz plasmon in a grating-gated graphene transistor

Bo Yan(闫博), Jingyue Fang(方靖岳), Shiqiao Qin(秦石乔), Yongtao Liu(刘永涛), Li Chen(陈力), Shuang Chen(陈爽), Renbing Li(李仁兵), Zhen Han(韩震)
Chin. Phys. B . 2017, 26(9): 097802 . **doi:** 10.1088/1674-1056/26/9/097802

Different angle-resolved polarization configurations of Raman spectroscopy: A case on the basal and edge plane of two-dimensional materials

Xue-Lu Liu(刘雪璐), Xin Zhang(张昕), Miao-Ling Lin(林妙玲), Ping-Heng Tan(谭平恒)
Chin. Phys. B . 2017, 26(6): 067802 . **doi:** 10.1088/1674-1056/26/6/067802

Broadband tunability of surface plasmon resonance in graphene-coating silica nanoparticles

Zhe Shi(史哲), Yang Yang(杨阳), Lin Gan(甘霖), Zhi-Yuan Li(李志远)
Chin. Phys. B . 2016, 25(5): 057803 . **doi:** 10.1088/1674-1056/25/5/057803

Visible-to-near-infrared photodetector based on graphene–$MoTe_2$–graphene heterostructure*

Rui-Xue Hu(户瑞雪), Xin-Li Ma(马新莉), Chun-Ha An(安春华), and Jing Liu(刘晶)†

State Key Laboratory of Precision Measurement Technology and Instrument, School of Precision Instruments and Opto-electronics Engineering, Tianjin University, Tianjin 300072, China

(Received 30 May 2019; revised manuscript received 25 July 2019; published online 16 October 2019)

Graphene and transition metal dichalcogenides (TMDs), two-dimensional materials, have been investigated wildely in recent years. As a member of the TMD family, $MoTe_2$ possesses a suitable bandgap of ~ 1.0 eV for near infrared (NIR) photodetection. Here we stack the $MoTe_2$ flake with two graphene flakes of high carrier mobility to form a graphene–$MoTe_2$–graphene heterostructure. It exhibits high photo-response to a broad spectrum range from 500 nm to 1300 nm. The photoresponsivity is calculated to be 1.6 A/W for the 750-nm light under 2 V/0 V drain–source/gate bias, and 154 mA/W for the 1100-nm light under 0.5 V/60 V drain–source/gate bias. Besides, the polarity of the photocurrent under zero V_{ds} can be efficiently tuned by the back gate voltage to satisfy different applications. Finally, we fabricate a vertical graphene–$MoTe_2$–graphene heterostructure which shows improved photoresponsivity of 3.3 A/W to visible light.

Keywords: two-dimensional materials, van der Waals heterostructure, transition metal dichalcogenides (TMDs), graphene, photodetector

PACS: 78.20.Jq, 42.79.Hp, 42.70.Gi **DOI:** 10.1088/1674-1056/ab4576

1. Introduction

Two-dimensional (2D) materials, including graphene, black phosphorene (BP), and transition metal dichalcogenides (TMDs) and their heterostructures, have been intensively studied due to their potential applications in next-generation electronic and optoelectronic devices.[1–6] Graphene possesses ultrahigh carrier mobility and excellent mechanical properties, which gives rise to the discovery of several novel phenomena.[7,8] However, its zero bandgap limits its applications in logic and optoelectronic devices. BP and TMDs, on the other hand, exhibits reasonably high carrier mobility and suitable bandgap, thus the 2D material become promising candidates for photodetectors.[9,10] For example, Cao *et al.* prepared a high-performance photodetector based on BP/$InSe_2$ heterostructure with responsivity of 53.8 A/W recently.[11] Nevertheless, using graphene as the device electrodes may not only reduce the electrode contact barriers, but also improve the separation of photo-generated electron–hole pairs. Thus, the photodetector configuration that combines TMDs as the photo-interactive material and graphene as electrodes can efficiently enhance the photodetection performance. In addition, recent research shows that graphene–TMDs-based vertical heterostructures can further improve the performance in photodetection, including high photo-response, large quantum efficiency, and short response time.[12–14]

Among various photodetectors, infrared (IR) photodetectors are highly demanded in many applications, such as telecommunication, biological imaging, and remote sensing.[15,16] So far, most of photodetectors based on 2D materials work in the visible-wavelength range because of their large bandgap above 1.2 eV.[17] On the other hand, as a member of TMDs, $MoTe_2$ possesses a suitable bandgap of ~ 1.0 eV in its bulk form, which is a promising candidate for near infrared (NIR) photodetector. Recently, $MoTe_2$-based photodetectors with various structures have been investigated, however, most of them focused on detecting visible light instead of NIR. For example, a graphene–$MoTe_2$ heterojunction with a responsivity of 0.02 A/W at visible light was fabricated.[18] A $MoTe_2$ photodetector enhanced by photogating effect shows a responsivity of 50 mA/W for 637-nm light and 24 mA/W for 1060-nm light.[18]

Here in this paper, we fabricate a graphene–$MoTe_2$–graphene heterostructure-based photodetector by using the few-layer graphene flakes as the source and drain electrode, which shows good photoresponsivity under both visible and NIR light with a wide spectrum response from 500 nm to 1300 nm. The photoresponsivity of 1.6 A/W (at $V_{ds} = 2$ V/$V_{gs} = 0$ V) and 154 mA/W (at $V_{ds} = 0.5$ V/$V_{gs} = 60$ V) are reached for the 750-nm and 1100-nm light illuminations, respectively. Besides, the polarity of the photocurrent under zero V_{ds} can be efficiently tuned by V_{gs}. We also fabricate a vertical graphene–$MoTe_2$–graphene structure by sandwiching a $MoTe_2$ flake between two graphene flakes, which reaches an improved photoresponsivity of 3.3 A/W to 532-nm light illumination.

*Project supported by the National Natural Science Foundation of China (Grant No. 21405109) and the Seed Foundation of State Key Laboratory of Precision Measurement Technology and Instruments, China (Pilt No. 1710).

†Corresponding author. E-mail: jingliu_1112@tju.edu.cn

© 2019 Chinese Physical Society and IOP Publishing Ltd

2. Experiment

2.1. Device fabrication

All of the $MoTe_2$ and graphene flakes were mechanically exfoliated from the bulk crystals, which were then transferred onto a 285-nm SiO_2/p-doped Si substrate. All the electrodes were defined using e-beam lithography. The contacts were then made by sequentially depositing 100-nm Cr film and 30-nm Au film on the flake through e-beam evaporation, followed by a standard lift-off process to complete the device fabrication.

2.2. Characterizations

The electrical characteristics of the $MoTe_2$ based devices were inspected by a semiconductor parameter analyzer B1500 (Agilent, USA) in ambient conditions. The photovoltaic properties were measured by using AOTF-Pro laser and B1500, with tunable output wavelength and power, respectively. The optical power was calibrated by an optical power meter PM100D. The Raman spectra were tested by a Renishaw InVia Raman microscope through using 532-nm laser source. The atomic force microscope (AFM) images were taken with a Bruker Dimension Icon.

3. Results and discussion

3.1. Lateral heterostructure

Figure 1(a) shows the schematic diagram of the graphene/$MoTe_2$/graphene photodetector. The two graphene flakes are transferred on each side of a $MoTe_2$ flake as the source and drain contact, respectively. Cr/Au electrodes are further deposited to contact the two graphene flakes. In this configuration, two graphene–$MoTe_2$ junctions are formed and can be efficiently tuned by applying back gate voltage and drain–source bias. Figure 1(b) shows the optical image of the device with a scale bar of 5 μm. The thickness of the $MoTe_2$ and two graphene flakes are confirmed by AFM to be 15 nm,

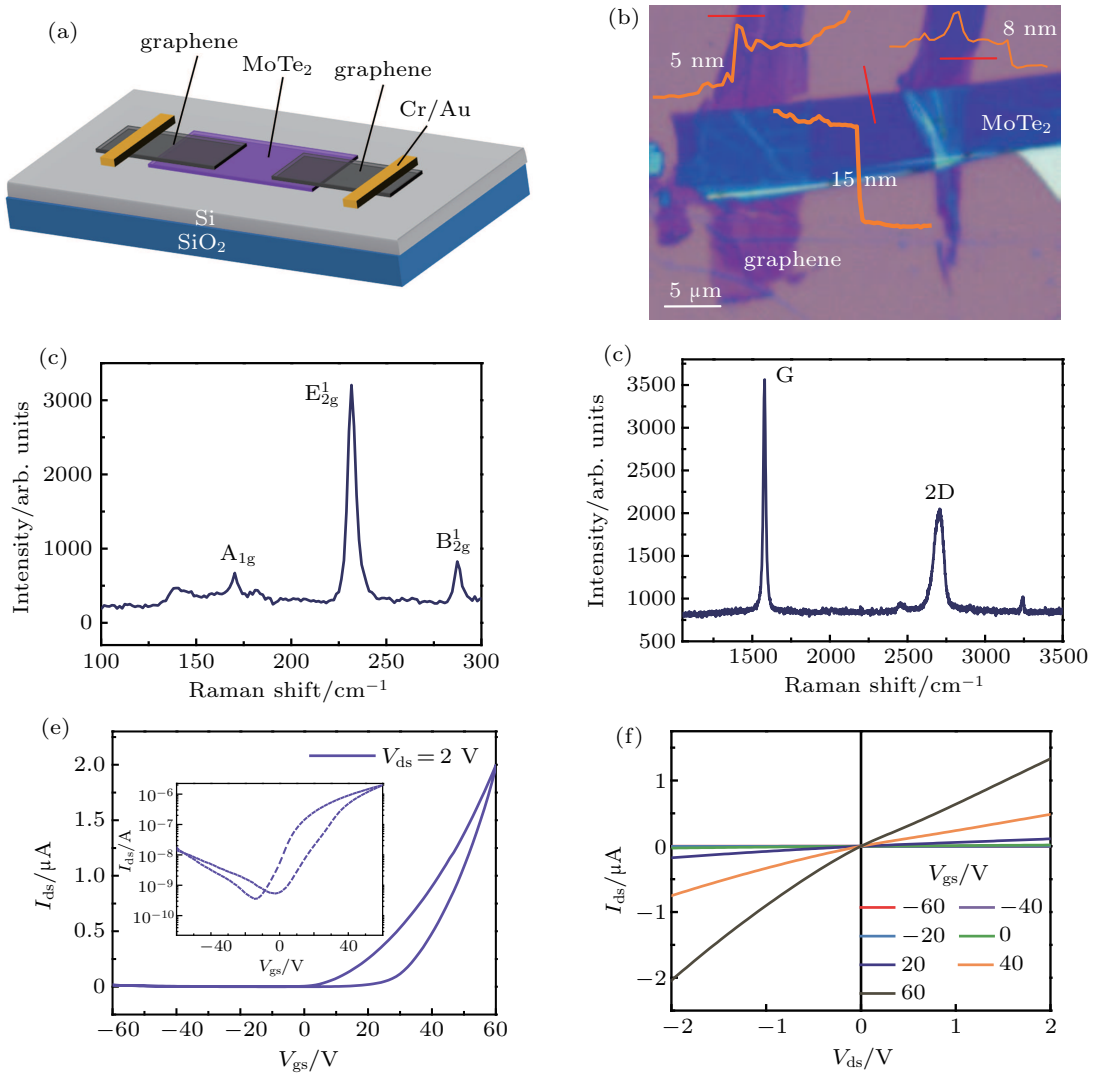


Fig. 1. (a) Schematic diagram of graphene–$MoTe_2$–graphene heterostructure. (b) Optical image of heterostructure, with scale bar being 5 μm. Thickness of $MoTe_2$ and two graphene are measured by AFM to be 15 nm, 5 nm, and 8 nm, respectively. (c) Raman spectra for $MoTe_2$, and (d) few-layer graphene in the heterostructure. (e) Transfer curve of the heterostructure on a linear scale. Inset shows transfer curve in logarithmic coordinate system. (f) Output characteristics of device.

5 nm and 8 nm, respectively. Figures 1(c) and 1(d) show the Raman spectra of $MoTe_2$ and graphene, respectively, which are consistent with previously reported results.[18] The transfer curve of the device is tested at a V_{ds} of 2 V and presented on a linear scale in Fig. 1(e), the inset of which shows the transfer curve in the logarithmic coordinate system. As the V_{gs} increases from −60 V to 60 V, the drain–source current (I_{ds}) first decreases and then increases, indicating an ambipolar behavior. The on-off ratio of the transfer characteristic reaches 10^4 with an on-state current of 2 μA. Figure 1(f) shows the output curves of the device under different values of V_{gs} (ranging from −60 V to 60 V), which is slightly asymmetric in the positive and negative V_{ds} regions, indicating the formation of the graphene–$MoTe_2$ junctions.

In Fig. 2, we investigate the dynamic photo response of the device to light illumination of wavelength in a range from 400 nm to 1400 nm under 1-V drain–source bias and 0-V gate bias. The incident power is fixed at 3.12 nW. Figure 2(a) presents the dynamic photocurrent of the device under the visible spectrum illumination in a wave length range from 400 nm to 750 nm. The larger photocurrent is observed for illumination wavelength greater than 500 nm, which reaches a peak value at 700 nm. The dynamic photoresponse of the device to near-infrared light with wavelength ranging from 800 nm to 1400 nm is exhibited in Fig. 2(b). Appreciable photoresponse is observed for light illumination with a wavelength shorter than 1300 nm. To further characterize the performance of the photodetector, we calculate its photoresponsivity from the equation of $R = I_{ph}/P$, where I_{ph} is the photocurrent and P is incident power focused on the device. Figure 2(c) shows the plots of the photoresponsivity of the device versus incident power. In general, the photoresponsivity of the device to visible light is larger than to NIR, with the maximum responsivity of 320 mA/W achieved at 750-nm light illumination. Furthermore, the response and recovery time of the device to 750-nm light illumination are both within 0.1 s as shown in Fig. 2(d). We also calculate the external quantum efficiency (EQE) of the device to be 52.8% from the equation of $\mathrm{EQE} = Rhc/(e\lambda)$, where e is the elementary charge, h is the Planck constant, λ is the wavelength of incident light, R is the responsivity of the device and c is the speed of light in air.

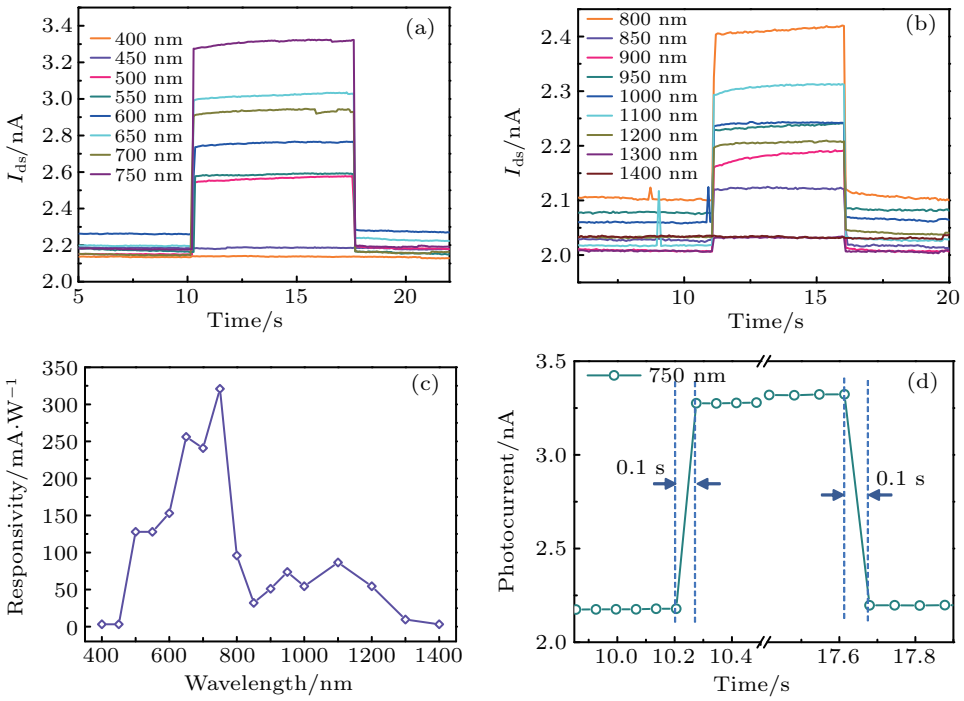


Fig. 2. Dynamic photoresponse of the device to (a) visible and (b) NIR light. (c) Photoresponsivity of the device *versus* incident light wavelength. (d) Response and recovery time of the device to 750-nm light illumination.

Figure 3 shows the further investigation of the photoresponse of the device to 1100-nm light illumination under different gate bias. As shown in Fig. 3(a), the photocurrent of the device varies with back gate voltage when the drain–source bias and incident light intensity are fixed at 0 V and 3.12 nW, respectively. Negative photocurrent is obtained when $V_{gs} < -20$ V, while the photocurrent shifts to positive value when $V_{gs} > -20$ V. This phenomenon can be explained by the energy band alignment between $MoTe_2$ and graphene. In the overlapped region, the energy band of $MoTe_2$ bends due to the difference in work function value between $MoTe_2$ and graphene, which results in the built-in potential to separate the photo-induced electron–hole pairs. Due to the difference between the areas of the overlapped regions and the contact mass, the built-in potential of the $MoTe_2$–graphene junctions formed at the two sides are asymmetric, resulting in the net

flow of photocurrent. When $V_{gs} < -20$ V, the Fermi level of $MoTe_2$ shifts to the valence band, the directions of built-in potential of the two junctions are shown in Fig. 3(c), leading a net current to flow from source to drain. When $V_{gs} > -20$ V, the directions of the built-in potential of the two junctions both shift to the opposite directions as shown in Fig. 3(d), causing the reversed net current to flow from drain to source. Figure 3(b) shows the photocurrent of the device under different back gate voltages when the drain–source bias is fixed at 0.5 V. When a positive voltage of V_{ds} is applied to the device, the photocurrent remains positive as the V_{gs} sweeps from −60 V to 60 V, the inset of which shows the enlarged area of V_{gs} ranging from −60 V to 0 V. This is because the external electrical field overcomes the difference between the built-in potentials on two sides, the schematic of which is shown in Fig. 3(e). Thus, the polarity and value of photocurrent can be efficiently tuned by adjusting the gate voltage and drain–source bias to meet various requirements. The photoresponsivity of the device reaches a highest value of 154 mA/W under a gate/drain–source bias of 60 V/0.5 V.

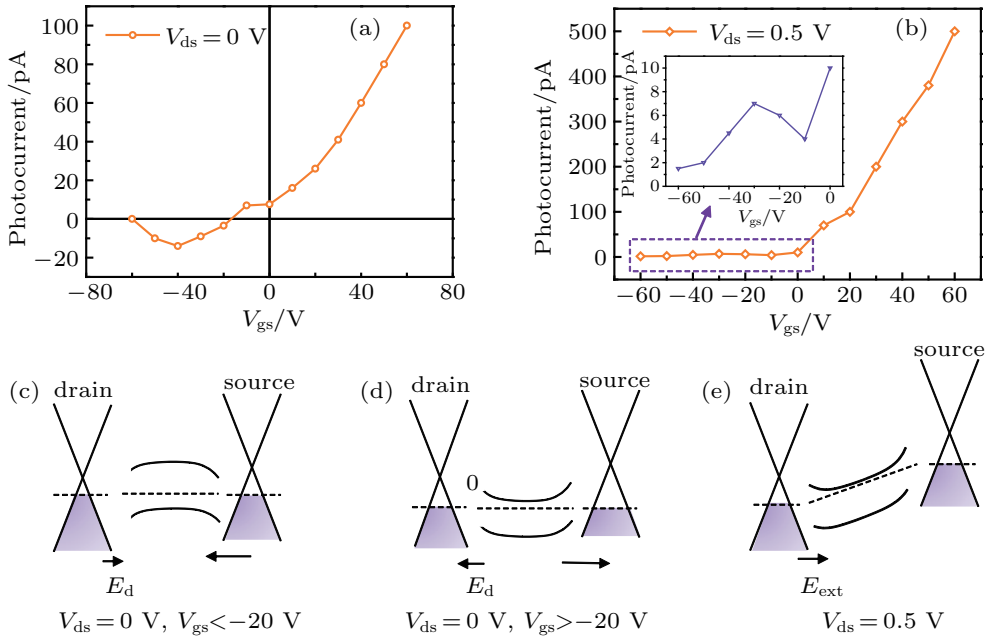


Fig. 3. Photocurrent *versus* V_{gs} at wavelength of 1100 nm for $V_{ds} = 0$ V (a) and 0.5 V (b). (c)–(e) Band alignment of the graphene–$MoTe_2$–graphene heterostructure at different values of V_{ds} and V_{gs} biases.

Figure 4 exhibits the photoresponse of the device to the 750-nm visible light. Figure 4(a) shows the output curves variation with incident light power ($V_{gs} = 0$). As expected, the output curve becomes steeper as the light incident power increases, which means that higher incident power generates more carriers under the same drain–source bias. According to Fig. 4(a), the maximum photoresponsivity reaches 1.6 A/W at a drain–source bias of 2 V and light incident power of 3.12 nW. Figure 4(b) summarizes the photocurrent and responsivity as a function of incident light power. With the increase of incident light, the photocurrent increases but the responsivity drops, for which the possible reason is that the photo-induced carriers are gradually saturated as the photon flux increases.[20] Figure 4(c) shows the photocurrent as a function of applied back gate voltage. Briefly, the photocurrent remains positive as the gate bias sweeps from −60 V to 60 V, which is consistent with the observation in Fig. 3(b). Moreover, the photocurrent increases as the gate voltage increases, which can be attributed to the reduction of channel conductance at high positive V_{gs}.

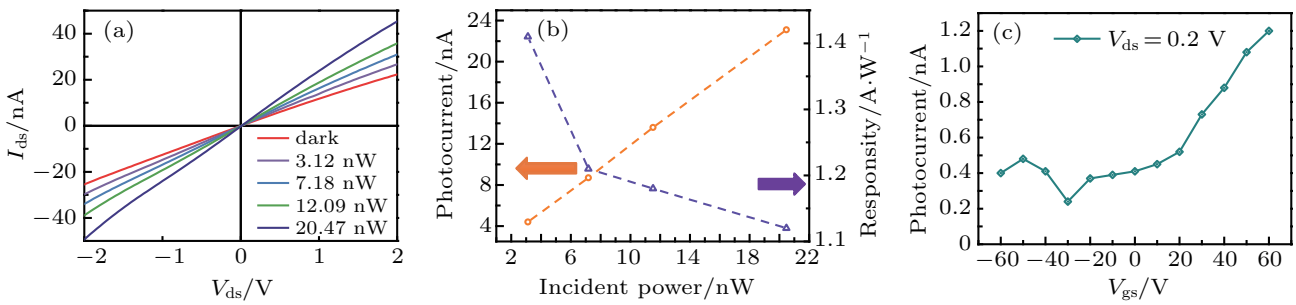


Fig. 4. Photoresponse of the device to 750-nm light. (a) Output characteristics of the device under 750-nm light illumination with different incident powers. (b) Photocurrent and responsivity as a function of incident power. (c) Photocurrent as a function of the back gate voltage.

3.2. Vertical heterostructure

We further fabricate a vertical heterostructure of graphene–$MoTe_2$–graphene by sandwiching a $MoTe_2$ flakebetween two graphene flakes, the schematic of which is shown in Fig. 5(a). It is guaranteed that the top graphene flake does not contact the bottom one. Two Cr/Au electrodes contact the top and bottom graphene flake, respectively. The optical image of this device is shown in Fig. 5(b), with a scale bar of 5 μm. Figure 5(c) shows the AFM image of the heterostructure. The thickness of $MoTe_2$, bottom and top graphene are measured to be 40 nm, 8 nm, and 15 nm, respectively, as shown in Figs. 5(c) and 5(d). The Raman spectra of the $MoTe_2$ and graphene flakes are exhibited in Figs. 5(e) and 5(f), respectively. The B^1_{2g} mode of bulk $MoTe_2$ is weaker than that of few-layer $MoTe_2$ as reported byYamamoto *et al.*[21] The transfer curves of the device under dark and light illumination at a drain–source bias of 0.2 V are shown in Fig. 5(g), exhibiting an ambipolar transport behavior. The device can be hardly turned off due to the atomically short channel (thickness of $MoTe_2$ flake). Under 550-nm light illumination with an incident power of 204 nW, the transfer curve shifts upward forabout 2 μA due to the increasing of transport carriers induced by the incident light, while the voltage of charge neutral point does not change under the illumination. Figure 5(h) shows the dynamic photoresponse of the device at a V_{ds} of 0.2 V. The curve shows good repeatability of the photoresponse, and exhibits a prominent photoresponsivity of 3.3 A/W.

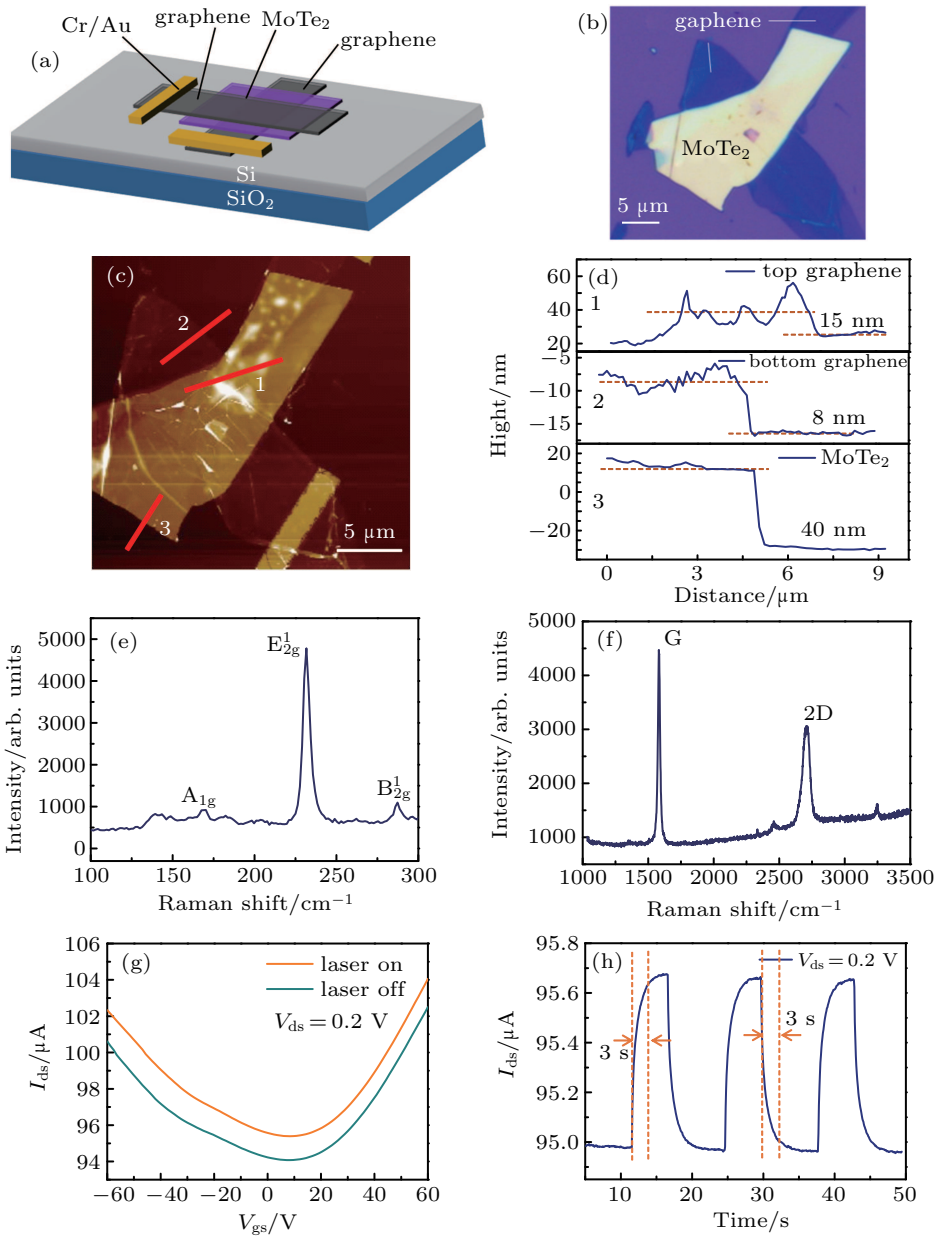


Fig. 5. (a) Schematic diagram of graphene–$MoTe_2$–graphene vertical vdWs heterostructure. (b) Optical image of heterostructure. The scale bar is 5 μm. (c) AFM image of vertical heterostructure. (d) Height profile of $MoTe_2$ and graphene flakes, measured at red lines marked in panel (c). Raman spectrum of (e) $MoTe_2$ and (f) graphene in vertical heterojunction. (g) Transfer curve of the device under dark and 550-nm light illumination. (h) Dynamic photoresponse of heterojunction at $V_{ds} = 0.2$ V.

4. Conclusions

In this work, we fabricatd a graphene–$MoTe_2$–graphene heterostructure photodetector with a nice performance of detecting light in a wide wavelength range from visible to near-infrared. The device shows a responsivity of 154 mA/W to the 1100-nm light under a gate/drain–source bias of 60 V/0.5 V, and 1.6 A/W for the 750-nm light under a gate/drain–source bias of 0 V/2 V, respectively. Besides, the polarity and value of the photocurrent can be tuned by the V_{gs} and V_{ds} to satisfy different requirements for applications. A vertical graphene–$MoTe_2$–graphene device structure is also demonstrated in this work, which shows increased photoresponsivity of 3.3 A/W to visible light with a wavelength of 532 nm under 0.2-V drain–source and zero voltage bias.

References

[1] Chao X, Mak C, Tao X and Feng Y 2016 *Adv. Funct. Mater.* **27** 1603886

[2] Sup C M, Deshun Q, Daeyeong L, Xiaochi L, Kenji W, Takashi T and Won Jong Y 2014 *ACS Nano* **8** 9332

[3] Butler S Z, Hollen S M, Linyou C, Yi C, Gupta J A, Gutiérrez H R, Heinz T F, Seung Sae H, Jiaxing H and Ismach A F 2013 *ACS Nano* **7** 2898

[4] Liu Y, Cai Y, Gang Z, Zhang Y W and Ang K W 2017 *Adv. Funct. Mater.* **27** 1604638

[5] Huang M, Wang M, Chen C, Ma Z, Li X, Han J and Wu Y 2016 *Adv. Mater.* **28** 3481

[6] Liu Y, Shivananju B N, Wang Y, Zhang Y, Yu W, Xiao S, Sun T, Ma W, Mu H and Lin S 2017 *Acs Appl. Mater. Interfaces* **9** 36137

[7] Young A F and Kim P 2009 *Nat. Phys.* **5** 222

[8] Wu X, Hu Y, Ming R, Madiomanana N K, Hankinson J H, Sprinkle M, Berger C and Heer W A D 2009 *Appl. Phys. Lett.* **95** 223108

[9] Fucai L, Hidekazu S, Hui S, Thangavel K, Viktor Z, Neil D, Fal'Ko V I and Katsumi T 2014 *ACS Nano* **8** 752

[10] Su G, Hadjiev V G, Loya P E, Zhang J, Lei S, Maharjan S, Dong P, P M A, Lou J and Peng H 2014 *Nano Lett.* **15** 506

[11] Cao R, Wang H D, Guo Z N, Sang D K, Zhang L Y, Xiao Q L, Zhang Y P, Fan D D Y, Li J Q and Zhang H 2019 *Adv. Opt. Mater.* **7** 1900020

[12] Tang H L, Chiu M H, Tseng C C, Yang S H, Hou K J, Wei S Y, Huang J K, Lin Y F, Lien C H and Li L J 2017 *ACS Nano* **11** 12817

[13] Shim J, Kim H S, Shim Y S, Kang D H, Park H Y, Lee J, Jeon J, Jung S J, Song Y J and Jung W S 2016 *Adv. Mater.* **28** 5293

[14] Hua X, Juanxia W, Qingliang F, Nannan M, Chunming W and Jin Z 2014 *Small* **10** 2300

[15] Gobin A M, Lee M H, Halas N J, James W D, Drezek R A and West J L 2007 *Nano Lett.* **7** 1929

[16] Gerasimos K and Sargent E H 2010 *Nat. Nanotechnol.* **5** 391

[17] Mak K F and Jie S 2016 *Nat. Photon.* **10** 216

[18] Kuiri M, Chakraborty B, Paul A, Das S, Sood A K and Das A 2016 *Appl. Phys. Lett.* **108** 063506

[19] Huang H, Wang J, Hu W, Liao L, Wang P, Wang X, Gong F, Chen Y, Wu G and Luo W 2016 *Nanotechnology* **27** 445201

[20] Gao Z, Jin W, Zhou Y, Dai Y, Yu B, Liu C, Xu W, Li Y, Peng H, Liu Z and Dai L 2013 *Nanoscale* **5** 5576

[21] Yamamoto M, Wang S T, Ni M, Lin Y F, Li S L, Aikawa S, Jian W B, Uneo K, Wakabayashi K and Tsukagoshi K 2014 *ACS Nano* **8** 3895